Revealing the Mechanistic Features of an Electrosynthetic Catalytic Reaction and the Role of Redox Mediators through DFT Calculations and Microkinetic Modeling

Marina Díaz-Ruiz,[a,b] Marc Nieto-Rodríguez,[a,b] Feliu Maseras *[a]

[a] Institute of Chemical Research of Catalonia (ICIQ-CERCA), The Barcelona Institute of Science and Technology, Avgda. Països Catalans 16, 43007, Tarragona, Spain.
E-mail: fmaseras@iciq.es

[b] Departament de Química Física i Inorgànica, Universitat Rovira i Virgili, Marcel·lí Domingo s/n, Tarragona 43007, Spain.

Supporting information for this article is given via a link at the end of the document.

Abstract: Organic electrosynthesis is an emerging field that provides original selectivity while adding features of atom economy, sustainability, and selectivity. Electrosynthesis is often enhanced by redox mediators or electroauxiliaries. The mechanistic understanding of organic electrosynthesis is however often limited by the low lifetime of intermediates and its difficult detection. In this work, we report a computational analysis of the mechanism of an appealing reaction previously reported by Mei and co-workers which is catalyzed by copper and employs iodide as redox mediator. Our scheme combines DFT calculations with microkinetic modeling and covers both the reaction in solution and the electrodic steps. A detailed mechanistic scheme is obtained which reproduces well experimental data and opens perspectives for the general treatment of these processes.

Introduction

The field of organic electrosynthesis has gained much importance during the last decades. A brand new reactivity is achieved, with high selectivities, functional group tolerances, and fewer side reactions.[1–7] The electric current, acting as an oxidant, can be a friendly alternative to chemical oxidants and allows the reaction to take place under milder conditions. The use of supporting species named redox mediators or electroauxiliaries has further expanded the range of electrochemical reactions.[8–10] Redox mediators are electrochemically active species that facilitate the oxidation/reduction of the substrate via indirect electrolysis (Figure 1). These species are more prone to be reduced/oxidized at the electrode than the substrate itself because of their mobility in solution and their lower redox overpotential.

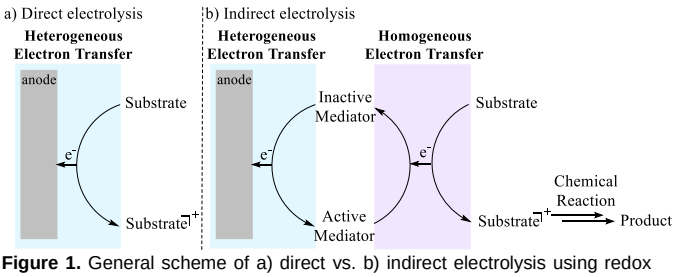

Figure 1. General scheme of a) direct vs. b) indirect electrolysis using redox mediators.

As a result, redox mediators are becoming more and more used in organic electrosynthesis. The most used redox mediators are: triarylamines,[11] hypervalent iodine,[12] N-oxyl radicals such as TEMPO,[13] halides,[14] metal salts,[15] and o-carboranes,[16] among others. Although its efficacy is unquestionable, the detailed operating mode of redox mediators is still poorly understood, as the general mechanism of organic electrosynthesis itself.

Computational chemistry has made significant contributions to homogeneous catalysis[17,18] and heterogeneous electrochemistry,[19] and has been shown to be a useful tool for a mechanistic understanding of complex processes involving intermediates difficult to identify experimentally. It seems a natural fit for organic electrosynthesis. However, the application of computational chemistry to this specific field has been limited. Earlier studies on electrocatalytic processes on surfaces[20] or in solution,[21,22] dealt with specific redox steps, in processes rather associated to traditional electrocatalysis. More modern applications have included cases closer to modern organic electrosynthesis, but still on rather simple cases, without a transition metal complex.[23,24] Finally, a number of more recent computational works have dealt with organic electrosynthesis processes, but only with specific chemical steps,[25–28] or with the estimation of the redox potential.[29,30] To the best of our knowledge, in no case there has been a systematic computational characterization of the full catalytic cycle at the level of detail that has become standard for other systems.[31,32]

We try to address this shortcoming in this work, where we have chosen for the computational study a representative reaction of organic electrosynthesis.[33] The reaction was reported in 2018 by the group of Mei and it involves an electrochemical copper-catalyzed reaction implicating a C-H amination, and uses iodide as mediator. The reaction conditions are summarized in Figure 2. In this context, the electricity and the redox mediator play an essential role that has not been fully characterized so far.

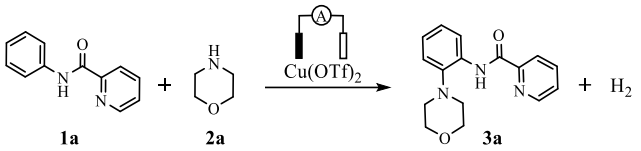

Figure 2. Reaction under study. 1a (0.2 mmol), 2a (4.0 equiv), Cu(OTf)2 (10 mol %), KOPiv (2.0 equiv), n-Bu4NI (50 mol %), and CH3CN (2 mL), in an undivided cell with two platinum electrodes (each 1.5 × 1.0 cm2), 27 °C, 3.0 mA, 24 h.

The reaction is carried out at room temperature, in acetonitrile solvent in an undivided cell. Copper triflate is the catalyst, potassium pivalate is used as an additive, and *n*-Bu_4NI as the redox mediator. The substrates are N-phenylpicolinamide (**1a**) and morpholine (**2a**), the latter in excess. The *ortho*-amination product (**3a)** is obtained in good yield (86%). The electrochemical reaction works for a large scope of N-arylpicolinamides and amines. In the exhaustive study of Prof. Mei and co-workers, they highlight that the reaction proceeds via SET, and that Cu(III) species are likely involved. Control experiments show that the reaction does not proceed without electricity, catalyst, mediator, or additive. Moreover, the change of iodide salt for the corresponding bromide precludes the reaction.

We aim to characterize here the mechanism of the reaction, including both the steps in solution and those in the electrodes. To do so, we combine the results of the DFT calculations with microkinetic simulations. This approach has been recently used in our group to successfully model other non-conventional processes such as ball-milling reactions.[34]

Results and Discussion

The reaction in solution

A significant part of the process is a copper-catalyzed reaction in solution, and this type of reactions has been the topic of computational homogeneous catalysis for years. The only caveat that we will have to take into account is that this reaction in solution is not self-contained. The reaction will generate pivalic acid units HOPiv, which will be consumed in the cathode, to produce pivalate anions $^-$OPiv, which will then be fed into the process. More critically, the presence of the iodide intermediate means that there will be oxidation steps which will consume iodine radicals $I_2^{\cdot-}$ (active mediator) and produce iodide anions I^-, which will then be processed at the anode. The anodic reaction will be further discussed in another section.

Even with these caveats, the reaction in solution is a multistep process far from trivial. We tried different alternatives, collected in the Supporting Information, and we settled on the simplified free energy profile presented in Figure 3. It has been divided in two parts which we discuss in order here. The starting copper species is $Cu(OTf)_2$ which spontaneously undergoes ligand exchange with two pivalates to give the precatalyst $Cu(OPiv)_2$. Then, one molecule of N-phenylpicolinamide **1a** coordinates to the copper species. Due to the acidity of **1a**, this coordination to copper involves one proton transfer to a pivalate ligand, which is released as pivalic acid. The conversion from the precatalyst to **int1** will not be barrierless, but we are not discussing it in detail because the associated ligand exchange and deprotonation steps are expected to be low barrier, will take place outside the catalytic cycle (see below) and will not have effect on the overall kinetics. Intermediate **int1** will evolve through the coordination of the morpholine substrate **2a**. The formed intermediate **int2** contains a deprotonated N-phenylpicolinamidate and one morpholine unit bound to a Cu(II) center, but seems to be a dead end. To move forward from **int2**, the participation of the iodine radical coming from the anodic reaction is necessary. The iodine radical is reduced to iodide, which brings oxidation of the N-phenylpicolinamidate ligand. The resulting complex, which would be cationic, takes a pivalate anion from the media to form the neutral species **int3**. Intermediate **int3** undergoes the deprotonation of the N-H bond of a morpholine unit, which takes place with an energy barrier of 9.9 kcal/mol in **TS3-4**. The proton from morpholine is transferred to a pivalate ligand, which departs the coordination sphere as pivalic acid. This pivalic acid will be ultimately reduced in the cathode to H_2 and pivalate anions, in a step that will be discussed on a next section. It is important to notice that there is a change in the spin state from triplet to singlet in the conversion from **int3** (T) to **TS3-4** (S). We were able to locate the minimum energy crossing point (MECP) associated to this spin change, and it has a lower energy than the TS, it is shown in the Supporting Information. It is also important to notice that this transformation could not take place without the prior oxidation step, this will be discussed in a section below. The species resulting from the N-H activation, **int4**, is a copper(II) complex with a morpholinyl ligand with a strong radical character. This complex undergoes the key step of the whole catalytic process, which is the formation of the C-N bond. This step takes place, always in the triplet spin state, through **TS4-5**, (its connectivity confirmed by IRC) which has an energy barrier of 17.9 kcal/mol. This is the most energetically demanding step of the reaction in solution. In this step, the formally anionic morpholinato ligand makes an electrophilic attack on the phenyl ring of the N-phenylpicolinamidate, which as a result loses its aromaticity.

The conversion from **int3** to **int5** is slightly endergonic and requires two barriers, the second one above 15 kcal/mol. This is the key part of the reaction, as the conversion from **int5** to the product, is a downhill process with low barriers. Intermediate **int5** must transfer the "excess" proton in the temporarily non-aromatic ring of the N-phenylpicolinamidate to the anionic nitrogen center coordinating to copper. This is accomplished using the pivalate ligand on copper as a shuttle and further stabilized by an additional morpholine molecule, through intermediates **int6** and **int7**. Product **3a** is released from **int7** resulting in intermediate **int8**. Then, **int8** is oxidized to **int9** which will coordinate one N-phenylpicolinamide molecule to start again the catalytic cycle from intermediate **int2**..

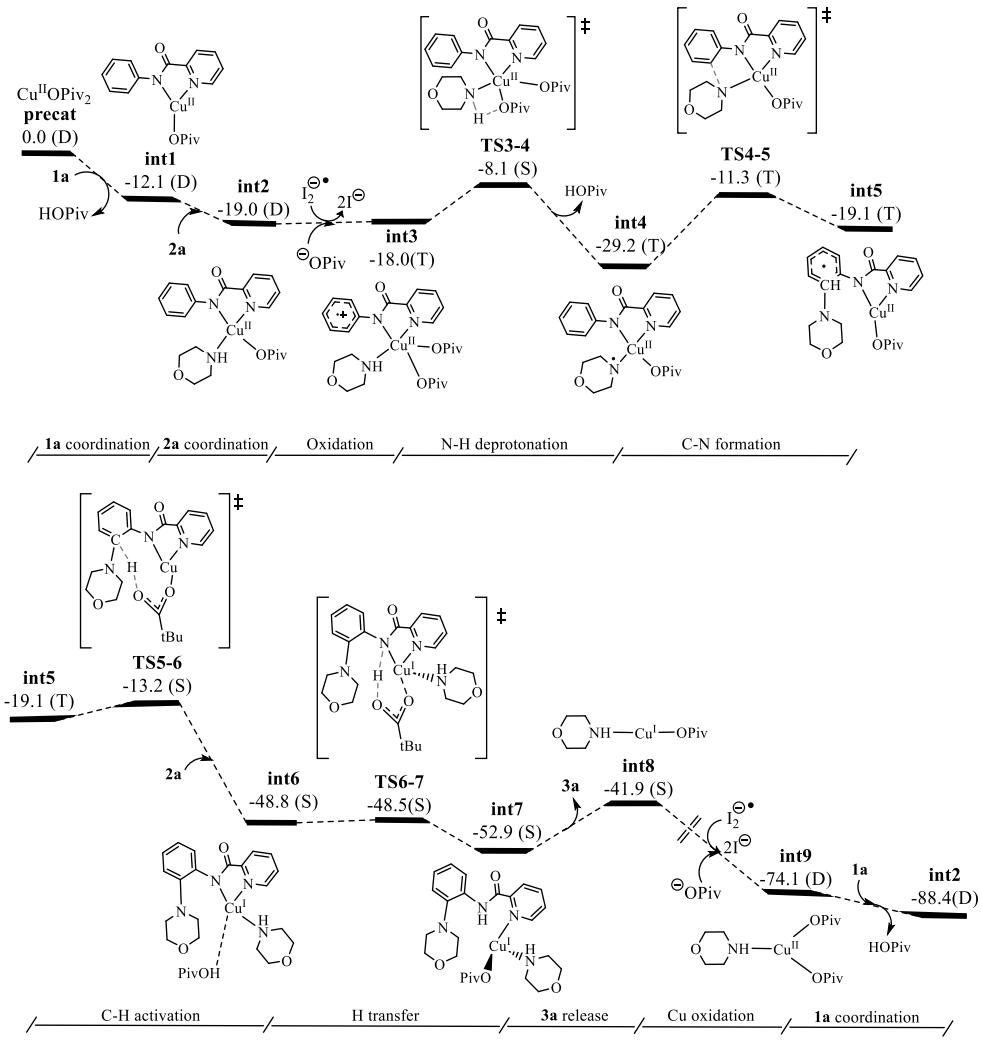

Figure 3. Free energy profile of the C-H amination of arenes using a copper catalyst. Level of calculation: B3LYP-D3/cc-pVTZ. Free energies in kcal/mol. Letters in parenthesis correspond to the multiplicity of each species: S for singlet, D for doublet, and T for triplet.

Further analysis of specific steps

Additional studies on the spin distribution have been carried out given that the reaction involves multiple changes in the spin state of the complexes. We have summarized the spin densities of different intermediates of the reaction in the following figure. Only the species with unpaired electrons are included (doublets and triplets).

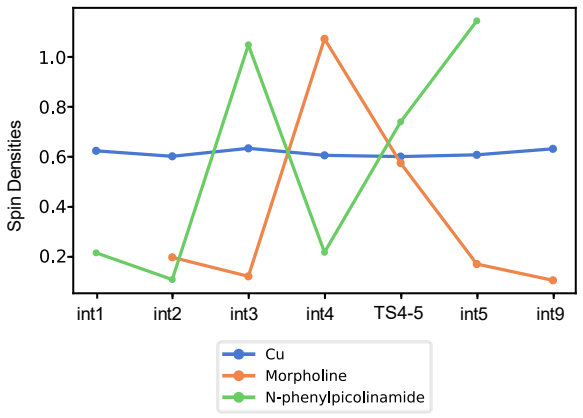

Figure 4. Spin densities of the different complexes.

As depicted in Figure 4, during these steps, the copper atom has always one unpaired electron (blue line), meaning that we have copper (II) complexes. On the other hand, the plot illustrates the oxidation of N-phenylpicolinamide substrate (in green) from int2 to int3, having one unpaired electron. Additionally, we can see that in the N-H protonation step (from int3 to int4) involves oxidation of the morpholine group, (orange line), which is reverted when the C-N bond is formed (int4 to int5).

Full catalytic cycle

The reaction in the previous section has reasonable barriers, but its connection to practical feasibility is not straightforward because the reaction is open-ended. Each reaction cycle consumes two iodine radicals and two pivalic acid molecules, and it generates four iodide and two pivalate anions. In order to operate, an engine will be necessary to transform these byproducts into the reactants for the next step. This engine is of course the electrodic reaction, and we have tried to represent the role of the two combined phases of the process in Figure 5. We notice here that we use diiodine radical anion, $I_2^{\cdot-}$ rather than monoatomic iodine radical $I^{\cdot}$ for stability reasons that will be discussed in the next section.

The outer cycle represents the chemical reaction, with the inner one representing the electrodic steps. Both of them are necessary for the overall process to take place. This graphical presentation has the advantage of emphasizing several key points: The first of them is the existence of the electrodic steps is necessary at different points in the catalytic cycle, pivalic acids are generated in some steps, and electrons are transferred to the electrodes in other steps. A second important aspect is that the function of the redox mediator is to facilitate the electrochemical oxidation by indirect electrolysis. As iodide is smaller than the copper complexes, it is easier for iodide to be transported to the electrode. Iodide is oxidized at the anode and then it takes the electron out of N-phenylpicolinamidate (**int2** to **int3**) or of copper (**int8** to **int9**). Hence, the oxidation of copper complexes is assisted by the reduction of the iodine radical species to iodide. The third and last aspect we want to remark is the role of pivalic acid in the cathodic reaction as a source for hydrogen gas and pivalate anion. In the reaction mixture, there is no pivalic acid, but it is generated during the reaction in solution. Without the formation of pivalic acid, the reaction could not take place because both anodic and cathodic reactions must work together.

The full catalytic cycle in Figure 5 gives a nice qualitative view of the full process. But in order to get a quantitative comparison between calculation and experiment we will need numerical estimations of the energetics involved in the electrodic reactions.

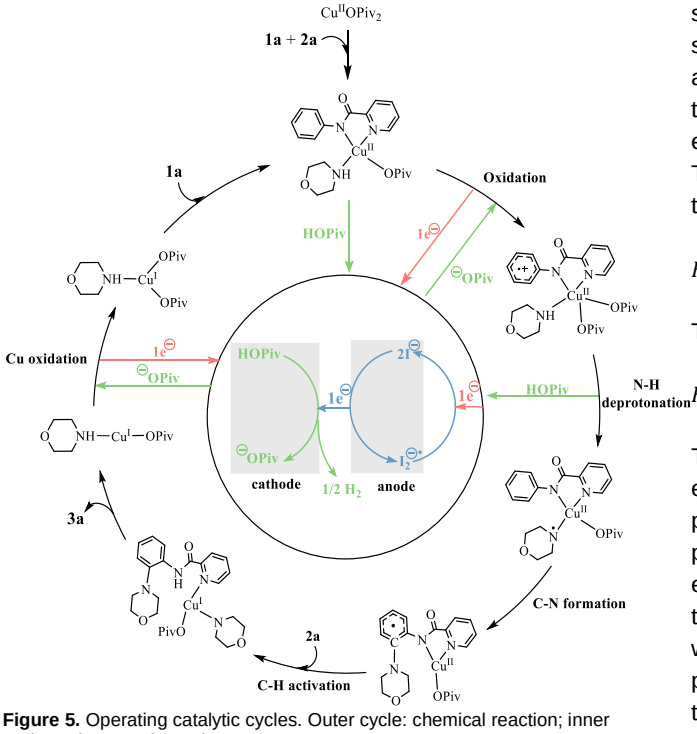

Figure 5. Operating catalytic cycles. Outer cycle: chemical reaction; inner cycle: redox transformation.

The electrodic reactions

This section focuses on the study of the reactions taking place at the electrodes. The electrodic reaction leads to the formation of the active mediator, which is an essential requirement to accomplish the oxidation of the complex, and therefore, continue with the reaction. To do so, it is necessary to oxidize the iodide anion and reduce the pivalic acid. Experiments show that this redox reaction can only take place under electrochemical conditions.

$$2 \cdot I^-(sol) + HOPiv(sol) \rightarrow I_2^{-\cdot}(sol) + OPiv^-(sol) + \frac{1}{2}H_2(g)$$

The phase of all the species is denoted in parenthesis: (s) for solid, (sol) for acetonitrile solution, (aq) for aqueous solution and (g) for gas. We notice that the equation above replaces the usually proposed monoatomic iodine radical $I^{\cdot}$ by the diiodine anion radical, $I_2^{-\cdot}$. The reason is purely thermodynamic; the free energy of the diatomic radical is 12.6 kcal/mol below the monoatomic one. Thus, direct use of the monoatomic radical would require a larger electric potential.

We will need the free energy cost of the reaction above to know about its feasibility. We see two major alternatives for its calculation. The first one is to compute directly with DFT the energy of all the species involved. This produces a value of 45.0 kcal/mol. However, this assumes an accurate reproduction of the role of hydrogen gas in the process, which is unlikely from this treatment. To address this concern, we favor a second alternative, which will be to separate the two semi-reactions and calculate their potential separately introducing as many available experimental data as possible in the process. It is important to mention that all the potential energies are referred to the standard hydrogen electrode (SHE) in water.

The cathodic reaction is the reduction of pivalic acid, HOPiv, to molecular hydrogen, H_2:

$$HOPiv\ (sol) + e^- \leftrightarrows\ OPiv^-(sol) + \frac{1}{2}H_2(g)$$

This reaction is closely related to the reaction of the SHE:

$$H^+(sol) + e^- \leftrightarrows\ \frac{1}{2}H_2(g)$$

The redox potential of the SHE in acetonitrile is experimentally known to be 0.240 V.[35] To obtain the potential for our reaction we need the concentration of protons in these conditions. In this way, we introduce the effect of pH in our reaction. As pivalic acid is a weak acid, this can be computed from the acidity constant as $\sqrt{Ka}$. We were not able to find an experimental value for the pKa of pivalic acid in acetonitrile, but we could extrapolate it from the reported pKa values in acetonitrile for a few carboxylic acids,[36,37] and the reported pKa values for these same acids and pivalic acid in water. We have carried out a linear regression leading to an estimated pKa for pivalic acid in acetonitrile of 23.83 (for further details see the Supporting Information). Using this value, the associated proton concentration and the Nernst equation, we obtain a value for the cathodic reduction potential of -0.465 V.

The anodic reaction is the oxidation of iodide to diiodine radical anion:

$$2 \cdot I^-(sol) \rightarrow I_2^{-\cdot}(sol) + e^-$$

We will divide it in three steps in order to compute its redox potential

$$I^-(aq) \rightarrow \frac{1}{2} I_2(s) + e^-$$

$$\frac{1}{2} I_2(s) \rightarrow I^{\cdot}(sol)$$

$$I^-(sol) + I^{\cdot} \rightarrow I_2^{-\cdot}(sol)$$

The redox potential in water of the first step above is known to be -0.536 V.[38] To translate this value into acetonitrile, we used the free energies in solution and we obtain -0.484 V. Our DFT calculations of the other two reactions in acetonitrile produce values of 18.1 and -12.6 kcal/mol, respectively. In order to be able to add redox potentials and free energies, we will use the following equation, obtaining values of -0.788 and 0.549 V, respectively.

$$\Delta G = -n \cdot F \cdot E$$

Adding the corresponding numbers for the three reactions above, we reach a value for oxidation in the anodic reaction of -0.723 V.
And the redox potential for the overall process is:

$$E_{total} = E_{reduction} + E_{oxidation} = -0.465 - 0.723 = -1.188\ V$$

Therefore, the theoretical potential of the redox reaction is -1.188 V. This value is a negative redox potential, meaning that we need to apply energy to carry out this reaction, which is in line with the evidence that the reaction does not proceed without an electric current. This redox potential means that the process is endergonic by 27.3 kcal/mol.

Microkinetic models and overpotential

We have computed in the previous section the redox potential associated to the chemical process, which we will label as thermodynamic potential, but there are other factors in the experimental set-up affecting the energy requirements for the electrochemical process. We summarize them in the equation below.

$$E_{effective} = E_{thermodyamic} + E_{applied} - E_{overpotential}$$

The effective potential is the "real" potential that can be felt by the system in solution, and that will give rise to free energy differences, equilibrium constants and ultimately to reaction rates. The external applied potential is introduced in the experimental system for the reaction to occur, and the overpotential is the required excess of voltage for the reaction to take place.[39] The experiment we intend to reproduce was carried out on galvanostatic conditions, thus with constant current, which means a fluctuating external potential. Luckily, the Supporting Information of the same publication reports additional experiments carried out under potentiostatic conditions. Those experiments found out that a 78% product yield is obtained with 0.800 V, and a 93% yield with 1.000 V. This gives us valuable information in order to estimate the overpotential of the process and, later, the applied potential for the main experiment at galvanostatic conditions.
In order to estimate the value, we will use microkinetic models. Free energy profiles give a lot of information on chemical processes, but they are limited in that they neglect the effects of concentration and time. Microkinetic models address these limitations.[40] To set up the microkinetic model, all the possible reactions and the energy barriers for direct and reverse processes are required. We have computed all of them and are reported in Table S3. For diffusion-controlled steps, we included a barrier of 3.5 kcal/mol (See the Supporting Information for details).[41]
To make an estimation of the overpotential, we tested different values and examined the predicted yield, which was then compared with data on potentiostatic experiments. Experimental data supplies values for external potentials of 0.600, 0.800, 1.000 V, with yield values of 0%, 78%, 93%, respectively. We manage to reproduce reasonably these values by assuming an overpotential of 0.540 V, as shown in Table 1. With this overpotential, the computed values are 0%, 79%, 100%.

Table 1. Estimation of the overpotential through the yields extracted from the microkinetic model.

Applied potential (V)	Experimental Yield (%)	Computed Yield (%)			
		Overpotential (V)			
		0.520	0.540	0.560	0.600
0.600	0	0	0	0	0
0.800	78	100	79	31	3
1.000	93	100	100	100	100

The overpotential values for electrocatalytic hydrogen evolution reactions vary depending on the catalyst, the electrolyte, the current density, etc. A wide range of overpotential values have been reported between 0.01 and 1.0 V, and our estimation fits well within these margins. [42–45] We took this estimated value of 0.540 V for overpotential, and applied it to the main experiment, which was carried out under galvanostatic conditions. We concluded that the applied potential had to be 0.820 V, and this produced a reaction yield of 89%, which is very close to the experimental result which is 86% isolated yield. Thus, we have been able to build a computational model that reproduces the available experimental data concerning reaction yield.
It is worth noticing that the estimated overpotential and applied potential lead to an estimated effective external potential of -0.908 V (-1.188 + 0.820 - 0.540), equivalent to 20.9 kcal/mol. This is the barrier that the process has to overcome, and is fully consistent with the rate-limiting step of process taking place at room temperature. The fact that the identity of the rate-limiting step was not obvious from Figure 3 further emphasizes the importance of carrying out microkinetic modelling for systems of this complexity.

Analysis of the microkinetic simulations

The microkinetic model reported above reproduces nicely the experimental yield after the reaction is completed. But it contains also a wealth of data on the evolution of concentrations of all species through time that contains further information of the reaction mechanism. We will exploit these results in this section. The computed data are summarized in Figures 6 and 7.

From Figure 6 we notice that the substrates **1a** and **2a** (green and red lines) are consumed while the product **3a** is formed (pink line). The change in concentration of substrate **2a** (red line) is not remarkable due to it is presence in excess.

The concentration of pivalate anion decreases from 0.20 to 0.18 M and remains constant during the reaction (in blue). Pivalic acid is generated arriving at a maximum of 0.01 M (in orange). The fact that the pivalate anion has a much higher concentration than the pivalic acid indicates basic conditions, in agreement with expectations. Regarding the concentration of the iodine-based mediator, we can observe that the concentration of the inactive mediator, I^- (in brown), is almost 0.05 M during all the reaction. The active mediator, $I_2^{\cdot-}$ (in purple), has a very low concentration of $1.65 \cdot 10^{-7}$ M, showing its high reactivity.

The fact that the concentrations of pivalate, pivalid acid, iodide and iodine radical are constant (stationary state) through the reaction time is a proof that these species are in equilibrium. Therefore, there is an equilibrium between the pivalate anion and pivalic acid, and another one between iodide and the iodine radical anion.

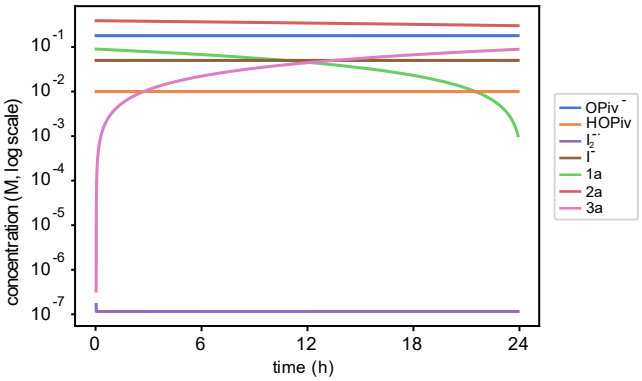

Figure 6. Time evolution of the concentration of pivalate anion, pivalic acid, iodide and diiodine radical anion. Y axis is represented in logarithmic scale.

The evolution of the copper species in solution is shown in Figure 7. All intermediates are present in tiny concentrations (below 10^{-5} M), except for **int2** (orange line), which is thus identified as the resting state. It corresponds to the Cu^{2+} complex with the two substrates coordinated (orange line).

Among other species, we can highlight those which change their concentrations through the course of the reaction, and are thus not in the stationary state. Intermediate **int9** (yellow line) is the final state, and its concentration increases when substrate **1a** is no longer available. Intermediates **int6** and **int7** (brown and pink lines) are in equilibrium with the product **3a**, and their concentrations increase with that of the product.

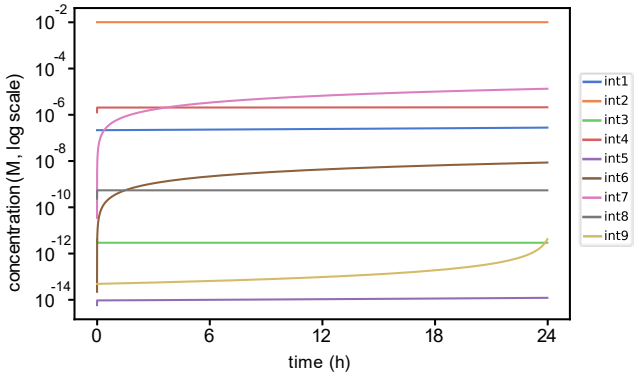

Figure 7. Time evolution of the concentration of all the copper intermediates. Y axis is represented in logarithmic scale.

Additional mechanistic studies

The main steps of the catalytic cycle are the N-H activation of the morpholine and the C-N bond formation, being the last one the rate-determining step. The computed mechanism is noticeably more detailed than what had been proposed in the experimental work, and clarifies some steps which were only suggested previously. We are going here to get further insights into these two transformations. In addition, we are going to discuss the use of bromide as mediator instead of iodide.

Neutral or oxidized complex in the N-H activation step. In the experimental suggestion, copper (III) species are involved in the main transformations along the catalytic cycle. mechanism. However, we have seen the copper centre is not oxidized to Cu(III), instead, the substrate **1a** is oxidized. We evaluate here what would happen if this was replaced by the copper(II) species before the substrate oxidation.

Figure 8 illustrates the free energy profile of the N-H activation for both species before and after oxidation. The purple path describes the activation with neutral species, which has an energy of 23.4 kcal/mol. For the generation of **int3**, **int2** is oxidized assisted by the reduction of diiodine radical. The N-H activation with the oxidized species (in teal) is more likely to happen with an energy barrier of almost 10 kcal/mol. Therefore, the N-H activation will take place with the oxidized complex.

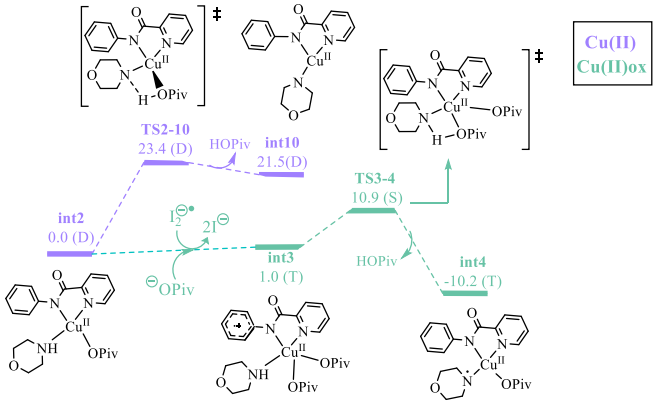

Figure 8. Free energy profile of the N-H activation with Cu^{2+} (purple) or oxidized Cu^{2+} (teal) species.

***Ortho*-selectivity in the C-N bond formation.** Regarding the selectivity of the reaction, we have compared the rate-determining step, which is the C-N formation, for *ortho*-, *meta*- and *para*-substituted arenes. Due to the spatial orientation of the complexes, the only product that can be formed is the *ortho* isomer with an accessible barrier of 17.9 kcal/mol (
Figure 9). *Meta* and *para* products cannot be formed because of the high energy barriers of 36.2 and 40.3 kcal/mol, respectively.

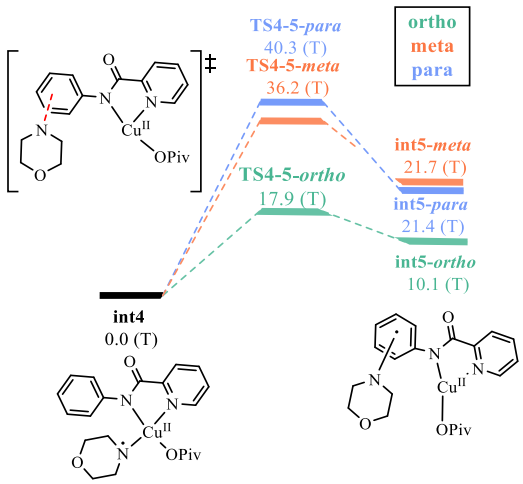

Figure 9. Free energy profile of the C-N bond formation step. *Ortho* in green, *meta* in orange, and *para* in blue.

Bromide as mediator. Mei and co-workers reported the reaction does not work when bromide replaces iodide as redox mediator. To rationalize this behavior, we have analyzed the redox reaction with bromide. Following the same procedure previously discussed, we have computed the redox potential for the anodic reaction.

$$2 \cdot Br^{-}(sol) \rightarrow Br_2^{-\cdot}(sol) + e^{-}$$

The resulting value is -0.974 V. This is 0.251 V more negative than the corresponding value for iodine (-0.723). Bromide is more difficult to oxidize, and this means that the applied potential should be about 0.250 V higher for the reaction to take place with similar efficiency. At such high applied potential, other undesired side reactions might take place.

Computational Details

Density Functional Theory (DFT) calculations have been carried out using Gaussian09 program.[46] The geometries have been optimized with B3LYP-D3[47,48] functional where D3[49] stands for Grimme dispersion GD3 with 6-31G(d)[50,51] basis set for the main group atoms and SDD for Cu (basis set I). Frequency calculations have been carried out to ensure the nature of the intermediates (no imaginary frequencies) and the transition states (one imaginary frequency which corresponds to the reaction coordinate). The Goodvibes software was used to obtain the free energy corrections with a frequency cut-off of 100cm^{-1} and a reference state correction from gas phase (1 atm) to solution phase (1 M). All the potential energies have been refined with single-point calculations using a larger basis set: cc-pVTZ[52] for all the atoms (basis set II). The Solvation Model based on Density (SMD)[53] has been used to simulate the solvent, acetonitrile, in all the calculations. All the reported energies are free energies in solution at 298.15K.

The pyssian library[54] has been used for the generation of input files. The minimum energy crossing points have been identified using a self-contained python script[55] that wraps the original J. N. Harvey's Fortran code.[56] Microkinetic simulations have been carried out using the COPASI 4.34 program.[57] The Python library copasi-helper[58] has been used to simplify the creation of the microkinetic models. A collection of computational results is available in the ioChem-BD repository,[59] and can be accessed via https://doi.org./10.19061/iochem-bd-1-299.

Conclusions

We have reported a full computational characterization through DFT and microkinetic modelling of the mechanism for a copper-catalyzed electrosynthetic arylation involving morpholine. Our study includes the electrodic reactions and an estimation of the required overpotential. The mechanism is best viewed as composed by two interconnected catalytic cycles: one for the chemical reaction, and the other for the electrochemical transformation mediated by the iodide. All available experimental data are reproduced, the key electroactive species linking the electrodic and the chemical cycles are identified, and further insight on the mechanism is gained from the analysis of the evolution of all intermediates through time. To the best of our knowledge, this is the first time an organic electrosynthesis process has been characterized with this level of detail. This work paves the way for further studies on organic electrosynthesis.

Acknowledgements

We acknowledge financial support from the CERCA Programme/Generalitat de Catalunya, MCIN/AEI (PID2020-112825RB-I00 and CEX2019-000925-S), and FEDER funds. This publication is part of the Grant (PRE2021-097618), funded by MCIN/AEI/10.13039/ 501100011033 and by the FSE+.

Keywords: organic electrosynthesis • microkinetic modeling • DFT calculations • catalysis • copper

[1] C. A. Malapit, M. B. Prater, J. R. Cabrera-Pardo, M. Li, T. D. Pham, T. P. McFadden, S. Blank, S. D. Minteer, *Chem. Rev.* **2022**, *122*, 3180.
[2] K.-J. Jiao, Y.-K. Xing, Q.-L. Yang, H. Qiu, T.-S. Mei, *Acc. Chem. Res.* **2020**, *53*, 300.
[3] A. Wiebe, T. Gieshoff, S. Möhle, E. Rodrigo, M. Zirbes, S. R. Waldvogel, *Angew. Chem. Int. Ed.* **2018**, *57*, 5594.
[4] M. C. Leech, K. Lam, *Nat. Rev. Chem.* **2022**, *6*, 275.
[5] R. Francke, R. D. Little, *Chem. Soc. Rev.* **2014**, *43*, 2492.
[6] M. C. Leech, A. D. Garcia, A. Petti, A. P. Dobbs, K. Lam, *React. Chem. Eng.* **2020**, *5*, 977.
[7] L. F. T. Novaes, J. Liu, Y. Shen, L. Lu, J. M. Meinhardt, S. Lin, *Chem. Soc. Rev.* **2021**, *50*, 7941.
[8] A. G. Tamirat, X. Guan, J. Liu, J. Luo, Y. Xia, *Chem. Soc. Rev.* **2020**, *49*, 7454.
[9] W. Shao, B. Lu, J. Cao, J. Zhang, H. Cao, F. Zhang, C. Zhang, *Chem. – Asian J.* **2023**, *18*, e202201093.

[10] A. G. Reid, C. W. Machan, *J. Am. Chem. Soc.* **2023**, *145*, 2013.
[11] C.-Y. Cai, X.-M. Shu, H.-C. Xu, *Nat. Commun.* **2019**, *10*, 4953.
[12] S. Doobary, D. L. Poole, A. J. J. Lennox, *J. Org. Chem.* **2021**, *86*, 16095.
[13] J. E. Nutting, M. Rafiee, S. S. Stahl, *Chem. Rev.* **2018**, *118*, 4834.
[14] F. Lian, K. Xu, C. Zeng, *Chem. Rec.* **2021**, *21*, 2290.
[15] N. Fu, G. S. Sauer, A. Saha, A. Loo, S. Lin, *Science* **2017**, *357*, 575.
[16] K. Hosoi, S. Inagi, T. Kubo, T. Fuchigami, *Chem. Commun.* **2011**, *47*, 8632.
[17] I. Funes-Ardoiz, F. Schoenebeck, *Chem* **2020**, *6*, 1904.
[18] J. N. Harvey, F. Himo, F. Maseras, L. Perrin, *ACS Catal.* **2019**, *9*, 6803.
[19] X. Liao, R. Lu, L. Xia, Q. Liu, H. Wang, K. Zhao, Z. Wang, Y. Zhao, *Energy Environ. Mater.* **2022**, *5*, 157.
[20] X. Crispin, R. Lazzaroni, V. Geskin, N. Baute, P. Dubois, R. Jérôme, J. L. Brédas, *J. Am. Chem. Soc.* **1999**, *121*, 176.
[21] P. Audebert, J.-M. Catel, G. Le Coustumer, V. Duchenet, P. Hapiot, *J. Phys. Chem. B* **1998**, *102*, 8661.
[22] E. V. Patterson, C. J. Cramer, D. G. Truhlar, *J. Am. Chem. Soc.* **2001**, *123*, 2025.
[23] C. L. Hammill, B. B. Noble, P. L. Norcott, S. Ciampi, M. L. Coote, *J. Phys. Chem. C* **2019**, *123*, 5273.
[24] H. Wang, H. Zhu, R. Guo, Q. Hu, S. Zeng, J. Lu, *Asian J. Org. Chem.* **2017**, *6*, 1380.
[25] W.-J. Kong, L. H. Finger, A. M. Messinis, R. Kuniyil, J. C. A. Oliveira, L. Ackermann, *J. Am. Chem. Soc.* **2019**, *141*, 17198.
[26] S.-K. Zhang, J. Struwe, L. Hu, L. Ackermann, *Angew. Chem. Int. Ed Engl.* **2020**, *59*, 3178.
[27] D.-Y. Wang, Y. Si, W. Guo, Y. Fu, *Nat. Commun.* **2021**, *12*, 3220.
[28] Y.-K. Xing, X.-R. Chen, Q.-L. Yang, S.-Q. Zhang, H.-M. Guo, X. Hong, T.-S. Mei, *Nat. Commun.* **2021**, *12*, 930.
[29] C. Zhu, M. Stangier, J. C. A. Oliveira, L. Massignan, L. Ackermann, *Chem. – Eur. J.* **2019**, *25*, 16382.
[30] Y. Kawamata, J. C. Vantourout, D. P. Hickey, P. Bai, L. Chen, Q. Hou, W. Qiao, K. Barman, M. A. Edwards, A. F. Garrido-Castro, J. N. deGruyter, H. Nakamura, K. Knouse, C. Qin, K. J. Clay, D. Bao, C. Li, J. T. Starr, C. Garcia-Irizarry, N. Sach, H. S. White, M. Neurock, S. D. Minteer, P. S. Baran, *J. Am. Chem. Soc.* **2019**, *141*, 6392.
[31] A. Lledós, *Eur. J. Inorg. Chem.* **2021**, *2021*, 2547.
[32] N. Fey, J. M. Lynam, *WIREs Comput. Mol. Sci.* **2022**, *12*, e1590.
[33] Q.-L. Yang, X.-Y. Wang, J.-Y. Lu, L.-P. Zhang, P. Fang, T.-S. Mei, *J. Am. Chem. Soc.* **2018**, *140*, 11487.
[34] B. S. Pladevall, A. Aguirre, F. Maseras, *ChemSusChem* **2021**, *14*, 2763.
[35] C. P. Kelly, C. J. Cramer, D. G. Truhlar, *J. Phys. Chem. B* **2007**, *111*, 408.
[36] A. Kütt, I. Leito, I. Kaljurand, L. Sooväli, V. M. Vlasov, L. M. Yagupolskii, I. A. Koppel, *J. Org. Chem.* **2006**, *71*, 2829.
[37] Z. Zhu, M. Odagi, N. Supantanapong, W. Xu, J. Saame, H.-U. Kirm, K. A. Abboud, I. Leito, D. Seidel, *J. Am. Chem. Soc.* **2020**, *142*, 15252.
[38] A. J. Bard, R. Parsons, J. Jordan, *Standard Potentials in Aqueous Solution*, 1st ed., Routledge, **2017**.
[39] J. E. Nutting, J. B. Gerken, A. G. Stamoulis, D. L. Bruns, S. S. Stahl, *J. Org. Chem.* **2021**, *86*, 15875.
[40] M. Besora, F. Maseras, *WIREs Comput. Mol. Sci.* **2018**, *8*, e1372.
[41] R. Pérez-Soto, M. Besora, F. Maseras, *Org. Lett.* **2020**, *22*, 2873.
[42] S. Wang, A. Lu, C.-J. Zhong, *Nano Converg.* **2021**, *8*, 4.
[43] A. M. Appel, M. L. Helm, *ACS Catal.* **2014**, *4*, 630.
[44] N. Jameei Moghaddam, M. Gil-Sepulcre, J.-W. Wang, J. Benet-Buchholz, C. Gimbert-Suriñach, A. Llobet, *Inorg. Chem.* **2022**, *61*, 16639.
[45] G. A. N. Felton, R. S. Glass, D. L. Lichtenberger, D. H. Evans, *Inorg. Chem.* **2006**, *45*, 9181.
[46] M. J. Frisch, G. W. Trucks, H. B. Schlegel, G. E. Scuseria, M. A. Robb, J. R. Cheeseman, G. Scalmani, V. Barone, B. Mennucci, G. A. Petersson, H. Nakatsuji, M. Caricato, X. Li, H. P. Hratchian, A. F. Izmaylov, J. Bloino, G. Zheng, J. L. Sonnenberg, M. Hada, M. Ehara, K. Toyota, R. Fukuda, J. Hasegawa, M. Ishida, T. Nakajima, Y. Honda, O. Kitao, H. Nakai, T. Vreven, J. A. Montgomery, Jr., J. E. Peralta, F. Ogliaro, M. Bearpark, J. J. Heyd, E. Brothers, K. N. Kudin, V. N. Staroverov, R. Kobayashi, J. Normand, K. Raghavachari, A. Rendell, J. C. Burant, S. S. Iyengar, J. Tomasi, M. Cossi, N. Rega, J. M. Millam, M. Klene, J. E. Knox, J. B. Cross, V. Bakken, C. Adamo, J. Jaramillo, R. Gomperts, R. E. Stratmann, O. Yazyev, A. J. Austin, R. Cammi, C. Pomelli, J. W. Ochterski, R. L. Martin, K. Morokuma, V. G. Zakrzewski, G. A. Voth, P. Salvador, J. J. Dannenberg, S. Dapprich, A. D. Daniels, Ö. Farkas, J. B. Foresman, J. V. Ortiz, J. Cioslowski, and D. J. Fox, Gaussian 09 (Gaussian, Inc., Wallingford CT, 2009)., .
[47] A. D. Becke, *J. Chem. Phys.* **1993**, *98*, 5648.
[48] C. Lee, W. Yang, R. G. Parr, *Phys. Rev. B* **1988**, *37*, 785.
[49] S. Grimme, *J. Comput. Chem.* **2006**, *27*, 1787.
[50] G. A. Petersson, A. Bennett, T. G. Tensfeldt, M. A. Al-Laham, W. A. Shirley, J. Mantzaris, *J. Chem. Phys.* **1988**, *89*, 2193.
[51] G. A. Petersson, M. A. Al-Laham, *J. Chem. Phys.* **1991**, *94*, 6081.
[52] T. H. Dunning, *J. Chem. Phys.* **1989**, *90*, 1007.
[53] A. V. Marenich, C. J. Cramer, D. G. Truhlar, *J. Phys. Chem. B* **2009**, *113*, 6378.
[54] R. Pérez-Soto, M. Besora, F. Maseras, *pyssian v.1.0.2*, **2021**.
[55] J. Rodríguez-Guerra, I. Funes-Ardoiz, F. Maseras, *EasyMECP v0.3.2.*, **2018**.
[56] J. N. Harvey, M. Aschi, H. Schwarz, W. Koch, *Theor. Chem. Acc.* **1998**, *99*, 95.
[57] S. Hoops, S. Sahle, R. Gauges, C. Lee, J. Pahle, N. Simus, M. Singhal, L. Xu, P. Mendes, U. Kummer, *Bioinformatics* **2006**, *22*, 3067.
[58] D. Garay-Ruiz, *copasi-helper*, **2022**.
[59] M. Álvarez-Moreno, C. de Graaf, N. López, F. Maseras, J. M. Poblet, C. Bo, *J. Chem. Inf. Model.* **2015**, *55*, 95.